Supporting Information

Dual-Gated Active Metasurface at 1550 nm with Wide (>300°) Phase Tunability

Ghazaleh Kafaie Shirmanesh[†], Ruzan Sokhoyan[†], Ragip A. Pala[†], and Harry A. Atwater[†‡*]

[†]Thomas J. Watson Laboratory of Applied Physics and [‡]Kavli Nanoscience Institute, California Institute of Technology, Pasadena, California 91125, United States

* Corresponding author. E-mail: haa@caltech.edu

1. Electrostatic simulations to extract ITO properties

To accurately calculate the optical response of metasurfaces under applied bias, we couple the device physics simulations (Device Lumerical) with finite difference time domain optical simulations (FDTD Lumerical). Our electrostatics calculations model the spatial distribution of charge carriers in the ITO layer embedded in the metasurface. In our device physics calculations, we assume that the work function of Al is 4.3 eV. We also assume that the effective electron mass of ITO is m^*=0.35 m_e, electron mobility of ITO is 25 $cm^2V^{-1}s^{-1}$, where m_e is the free electron mass. Since our ITO is degenerately doped, we assume that holes do not significantly contribute to the observed physical processes. In Device Lumerical software, we input that the effective mass of holes is $1\times m_e$, and the hole mobility is 1 $cm^2V^{-1}s^{-1}$. In our simulations, the bandgap of ITO is set to 2.8 eV,[1] and the electron affinity of ITO is chosen as 4.8 eV. The assumed DC permittivity of ITO is 9.3.[2] Once we have identified the spatial distribution of charge under different applied biases, we then relate the calculated carrier density to the complex dielectric permittivity of ITO ε_{ITO} by using the Drude model: $\varepsilon_{ITO} = \varepsilon_\infty - \omega_p^2/(\omega^2 + i\omega\Gamma)$. The plasma frequency ω_p is given by the following expression $\omega_p = \sqrt{N_{ITO}e^2/(\varepsilon_0 m^*)}$. Here, N_{ITO} is the carrier concentration of ITO, which we extract from the device physics calculations, e is the electron charge, ε_0 is the DC permittivity of vacuum, Γ is the damping constant, ε_∞ is a fitting constant, ω is the angular frequency, which is related to the wavelength λ as $\lambda=2\pi c/\omega$, where c is the speed of light in vacuum. When performing optical simulations, we assume that m^*=0.35 m_e, $\gamma = 1.8\times10^{14}$, and ε_∞=3.9. Figure S1a, b show the imaginary part of the permittivity of ITO for Case I and Case II, respectively.

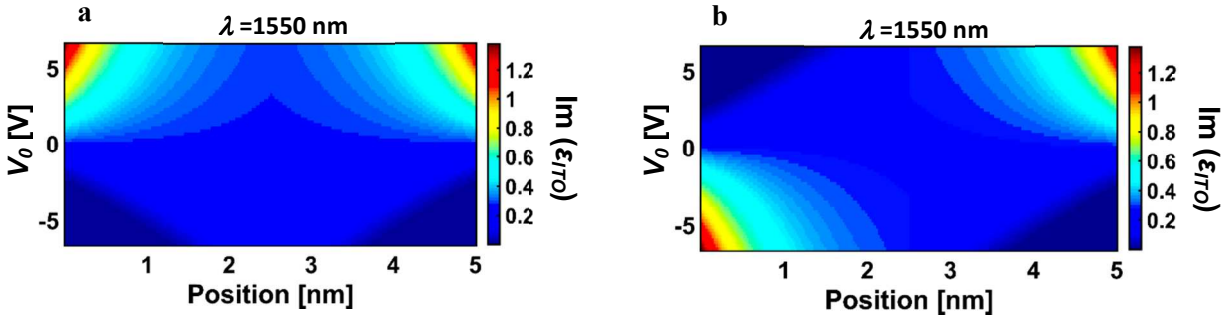

Figure S1. Calculated imaginary part of dielectric permittivity of a 5 nm-thick ITO film embedded in our dual-gated metasurface as a function of position and applied bias for (a) Case I and (b) Case II. Here, 0 nm corresponds to the bottom ITO/HAOL interface, and 5 nm corresponds to the top ITO/HAOL interface.

2. Fabrication and characterization of HfO_2/Al_2O_3 nanolaminate

We fabricate HfO_2-Al_2O_3 nanolaminate films by using atomic layer deposition (ALD). We perform the deposition at 150^{o}C by using thermal recipe in our ALD tool (Fiji G2 Plasma Enhanced Atomic Layer Deposition System). We use tetrakis (ethylmethylamino) hafnium, $[(CH_3)(C_2H_5)N]_4Hf$, as a precursor for Hf, while we use trimethyl aluminum, $Al(CH_3)_3$, as a precursor for Al. During our ALD process we use water as an oxidant. To fabricate HAOL, we adopt two growth periods with each period consisting of 10 cycles of Al_2O_3 and 30 cycles of HfO_2. Immediately after the deposition, we perform rapid thermal annealing (RTA) in nitrogen atmosphere. The RTA is performed for 30 seconds at a temperature of 600^{o}C. Previous research has shown that the RTA treatment causes the diffusion of Al atoms (from Al_2O_3 layer) into HfO_2, resulting in formation of Al-Hf-O bonds.[3]

To determine the growth per cycle rates of Al_2O_3 and HfO_2 films, we fabricate the Al_2O_3 and HfO_2 control samples on Si substrates. We use 2×10 cycles to grow Al_2O_3 and 2×30 cycles to grow HfO_2. We perform transmission electron microscopy (TEM) to identify the thicknesses of the grown samples. The thicknesses of the fabricated Al_2O_3, HfO_2, and HAOL films are 1.54 nm, 7.67 nm, and 9.46 nm, respectively (Figure S2). As shown in Figure 1f and Figures S2a, b, while Al_2O_3 and HfO_2 layers are amorphous, the HAOL layer is partially crystallized after RTA treatment. The TEM images indicate that, as expected, there is a thin native oxide layer formed on Si substrates. To enable electrical characterization of the dielectric films, we sputter Al top electrodes while using shadow masks. The continuous Al bottom electrodes are deposited by using electron beam evaporation. To identify the DC permittivities of the films, we use the capacitance–voltage (C–V) measurements of the fabricated metal–oxide–semiconductor MOS capacitors at 100 kHz. The DC permittivities of the fabricated Al_2O_3, HfO_2, and HAOL films are 10.5, 17.8, and 22, respectively. By using current–voltage (I–V) measurements performed on metal-oxide-metal (MIM) structures, we identify that the breakdown fields of the fabricated Al_2O_3, HfO_2, and HAOL films are 7.4 MV/cm, 3.1 MV/cm, and 7.2 MV/cm, respectively.

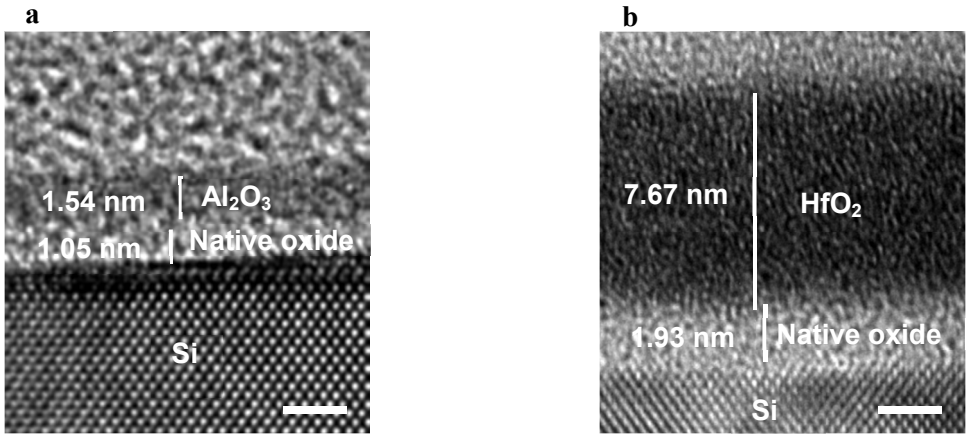

Figure S2. TEM images of (a) the Al_2O_3 control sample deposited via 20 ALD cycles and (b) the HfO_2 control sample deposited via 60 ALD cycles. Scale bar is 2 nm.

3. Fabrication and characterization of indium tin oxide (ITO)

We deposit our ITO films via room-temperature RF sputtering. The deposition pressure is 3 mTorr while the applied RF power is 48W. We strike the plasma by using Ar gas with the flow rate of 20 sccm. We vary the argon/oxygen gas (Ar/O_2:90/10) flow rate to achieve different carrier concentrations of ITO.[4, 5] In order to characterize the deposited ITO films, we perform Hall measurements and spectroscopic ellipsometry.[6] To this end, we sputter ITO films on quartz and silicon substrates by changing the $Ar+O_2$ flow rate while keeping other parameters constant. We identify that the deposition rate of ITO is about 1.11 nm/minute, when the mentioned deposition parameters are used. Thus, we sputter ITO for 4.5 minutes to obtain 5 nm-thick ITO films. Then we perform Hall measurements on the films deposited on quartz substrates, and we perform spectroscopic ellipsometry on the films deposited on silicon substrates. After obtaining the charge carrier concentration N_{ITO} and electron mobility μ of the ITO films from Hall measurements, and using the relation $\rho = \frac{1}{qN_{ITO}\mu} = \frac{m^* m_e}{N_{ITO}q^2\tau}$, we obtain the complex permittivity of the ITO films via an ellipsometry fit to a single Drude function $\varepsilon_{ITO} = \varepsilon_\infty - \frac{\omega_p^2}{\omega^2 + i\Gamma\omega}$. Here, Γ is the damping constant, and ω_p is the plasma frequency, which is related to the charge carrier density N_{ITO} via $\omega_p = \sqrt{\frac{N_{ITO}e^2}{\epsilon_0 m^*}}$. Here, e, ϵ_0, and m^* are the electron charge, the dielectric permittivity of vacuum, and the effective electron mass, respectively. The high-frequency permittivity ε_∞, damping rate Γ, and electron effective mass m^* are determined via fitting the Drude model to the measured ellipsometry data. Thus, the dielectric permittivity of ITO ε_{ITO} is related to the plasma frequency ω_p via Drude model, and the plasma frequency itself depends on the carrier concentration of ITO N_{ITO}. This fact is the key reason why the optical response of the metasurface is modulated under applied bias. The electrical and optical constants obtained from Hall measurements and spectroscopic ellipsometry are listed in Table S1.

When fabricating our dual-gated metasurface (see Supporting Information S5 for fabrication steps), we deposit HAOL on top of ITO. Since the HAOL layer needs to be RTA-treated at 600 ^{o}C for 30 seconds, we need to take into account the effect of the RTA treatment on properties of ITO. To investigate this effect, we fabricate two identical ITO samples and perform RTA treatment at 600^{o}C for 30 seconds on one of the samples. We do Hall measurements and ellipsometry on both samples and compare the results. As seen in Table S1, the fitted parameters are in good agreement with the expected final thicknesses of the films and literature values for the constants ($\Gamma = 0.1185$ eV, $m^* = 0.35\ m_e$ and $\epsilon_\infty = 3.9$), which we use to define the dielectric permittivity of ITO in our simulations.[5, 7, 8] We consider the bulk charge carrier concentration of ITO to be $N_{ITO} = 3\times10^{20}$ cm^{-3} which draws parallel to the plasma frequency of $\omega_p = 1.0874$ eV.

Table S1. Electrical and Optical parameters obtained from Hall measurements and spectroscopic ellipsometry for the ITO films deposited using different Ar+O_2 flows rates.

Ar+O_2 flow rate [sccm]	Fitted thickness [nm] as deposited	Fitted thickness [nm] after RTA	ϵ_∞ as deposited	ϵ_∞ after RTA	ω_p [eV] as deposited	ω_p [eV] after RTA	γ [eV] as deposited	γ [eV] after RTA
0	4.3637	4.3137	6.0853	5.8447	1.8516	1.924	0.16245	0.14188
0.4	5.3566	5.1242	6.4603	5.402	1.9679	1.2989	0.14092	0.12521
0.5	5.2988	5.3237	5.1834	4.8832	1.4075	0.94404	0.16379	0.12981
0.6	4.0852	6.4846	5.338	5.0306	1.4496	1.0185	0.15081	0.11095
0.7	5.5826	5.3170	5.9536	4.689±0	1.7932	0.86608	0.13828	0.1543
0.8	5.4923	5.8453	5.6552	5.1296	1.5872	1.1351	0.14384	0.14262
0.9	5.6060	5.5593	5.1672	5.6363	1.285	1.4352	0.14187	0.13105
1	6.2157	6.0063	5.5049	5.4699	1.4416	1.2529	0.13843	0.12189

When fabricating our metasurface we deposit ITO at Ar+O_2 flow rates of 0.6 sccm. In this case, the plasma frequency and the charge carrier concentration of ITO after RTA treatment is $\omega_p = 1.0185$ eV and $N = 2.6319\times10^{20}$ cm^{-3}, respectively. Note that after depositing top gate dielectric on ITO, the carrier concentration of ITO is expected to increase due to the leakage of oxygen from the ITO layer into the dielectric that occurs during ALD process.[9] As a result, we expect the carrier concentration of ITO in our final device to be slightly higher than the values we obtain via Hall measurements.

It should be noted that the smoothness of the ITO films incorporated into our metasurface is of great importance. To this end, we deposited different test samples using different sputtering powers and temperatures. To investigate the roughness of the deposited ITO films, we performed atomic forced microscopy (AFM) on our ITO samples and figured out that sputtering at room temperature with applied RF power of 48 W would result in the ITO films with an average root

mean square (RMS) roughness of ~0.3 nm. This was expected since having rough and porous ITO films would not let us perform Hall measurements and/or fit the ellipsometry results with Drude model.

4. Full wave simulation of tunable metasurface

The simulated reflectance spectra for different applied biases for Case I and Case II are presented in Figures S3a, b. Figures S3c, d show the spectra of relative reflectance change at different applied voltages for Case I and Case II, respectively. The insets of Figures S3c, d show the relative reflectance change as a function of applied voltage at a fixed wavelength of 1550 nm.

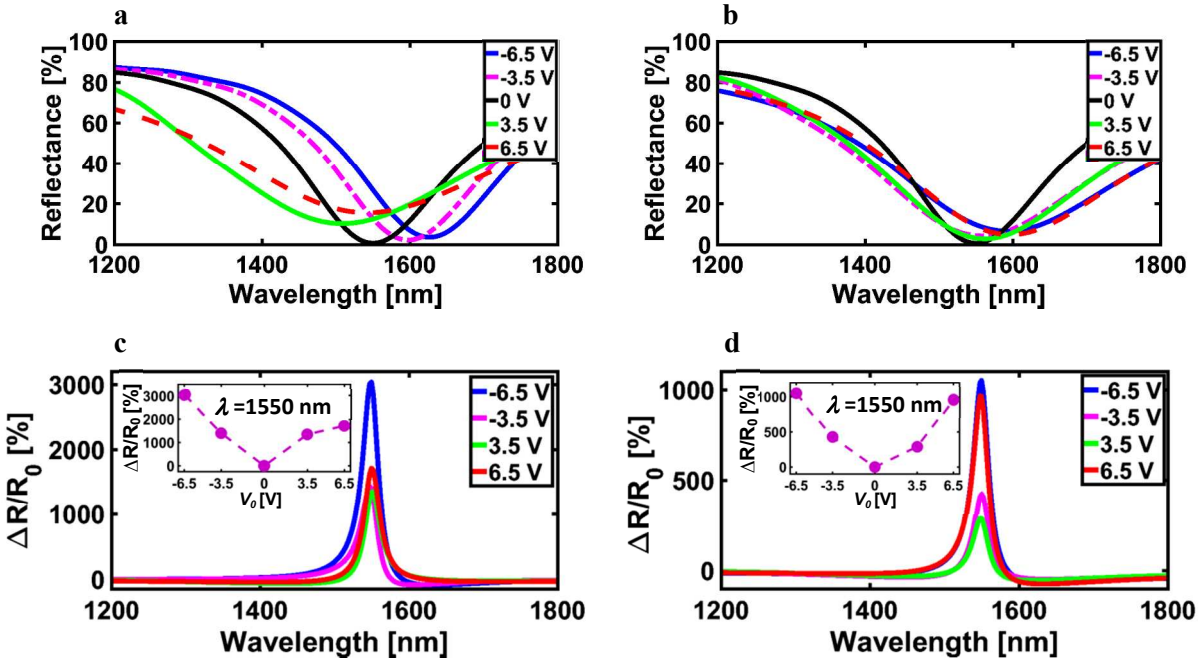

Figure S3. Reflectance spectrum for different applied biases for (a) Case I and (b) Case II. The relative reflectance change spectrum for different applied voltages for (c) Case I and (d) Case II. The insets show the relative reflectance change as a function of voltage at a wavelength of 1550 nm.

Figure S4 shows the spatial distribution of the z-component of the electric field E_z inside the dielectric spacer of the metasurface, which consists of HAOL/ITO/HAOL planar layers. The spatial distribution of E_z is calculated at a wavelength of λ =1550 nm. Figures S4a-c correspond to the bias application configuration that is referred to as Case I (Figure 2a), while Figures S4d-f correspond to the bias application configuration referred to as Case II (Figure 2d). Both in Case I and Case II the assumed values of the applied bias are V_0= −6.5 V, V_0=0 V and, V_0=6.5 V (for definition of V_0 see Figure 2). As seen in Figures S4c, d and f, there is a strong field enhancement at the interfaces of ITO and HAOL. Figure S4 also shows that the z component of the electric field E_z around right and left edges of the antenna are antiparallel to each other.

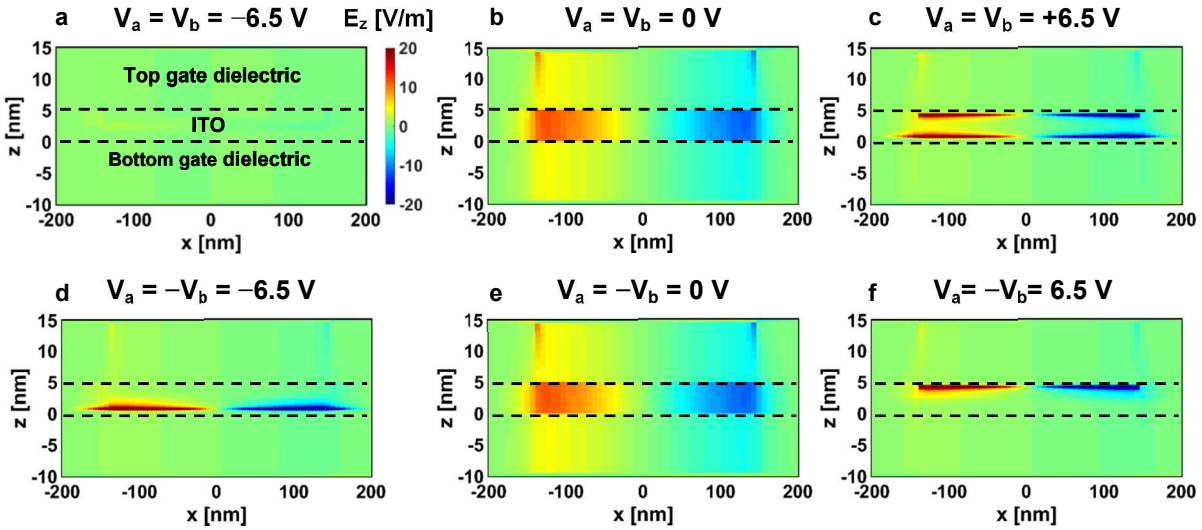

Figure S4. Close-up image of the spatial distribution of the z component of electric field in the HAOL/ITO/HAOL region for (a) $V_0 = -6.5$ V, (b) $V_0 = 0$, and (c) $V_0 = +6.5$ V in Case I, (d) $V_0 = -6.5$ V, (e) $V_0 = 0$ V, and (f) $V_0 = +6.5$ V in Case II.

Figure S5 plots the spatial distribution of the absolute value of the magnetic field for our dual-gated metasurfaces. Figures S5a-c correspond to Case I, while Figures S5d-f correspond to Case II. Both in Case I and Case II we assume the following values of applied bias voltages: $V_0 = -6.5$ V, $V_0 = 0$ V and, $V_0 = 6.5$ V. As seen in this figure, the magnetic field is localized in the gap region between the Al antenna and the back reflector. This proves the existence of a magnetic dipole resonance. One can also notice that the strength of the magnetic dipole is strongly altered by changing the applied voltage.

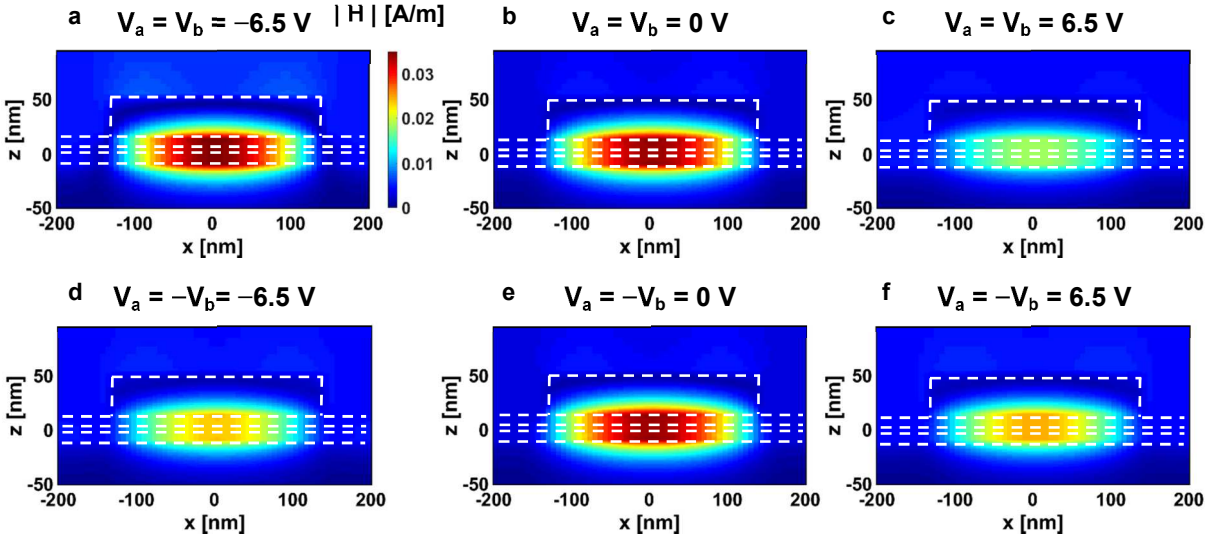

Figure S5. Spatial distribution of the magnitude of the magnetic field for (a) $V_0 = -6.5$ V in Case I, (b) $V_0 = 0$ V in Case I, (c) $V_0 = +6.5$ V in Case I, (d) $V_0 = -6.5$ V in Case II, (e) $V_0 = 0$ V in Case II, and (f) $V_0 = +6.5$ V in Case II. The dashed lines specify the boundaries between the back reflector and bottom HAOL, the bottom HAOL and the ITO layer, the ITO layer and the top HAOL, and, finally, the dashed lines outline the patch antenna.

5. Fabrication of double-gated tunable metasurface

In order to fabricate our gate-tunable metasurface, we first perform RCA1 cleaning (H_2O:NH_4OH:H_2O_2 = 5:1:1) of silicon substrates. Then by using e-beam evaporation, we deposit an 80 nm-thick aluminum back reflector. On top of the Al back reflector we deposit a 9.5 nm-thick HAOL by using ALD, as described in Supporting Information Part 2. We then deposit a 5 nm-thick ITO layer on top of the HAOL gate dielectric by using RF magnetron sputtering in Ar/O_2 plasma environment. Once we have sputtered the ITO layer, we deposit another 9.5 nm-thick HAOL layer. Afterwards, we spin e-beam resist on our Si/Al/HAOL/ITO/HAOL planar sample and pattern Al fishbone antenna arrays and contact pads via standard e-beam lithography. After developing the e-beam-exposed sample, we deposit Al by using e-beam evaporation. We obtain our fishbone dual-gated metasurface after performing lift-off process. Figure S6 summarizes the described fabrication steps of our tunable metasurface.

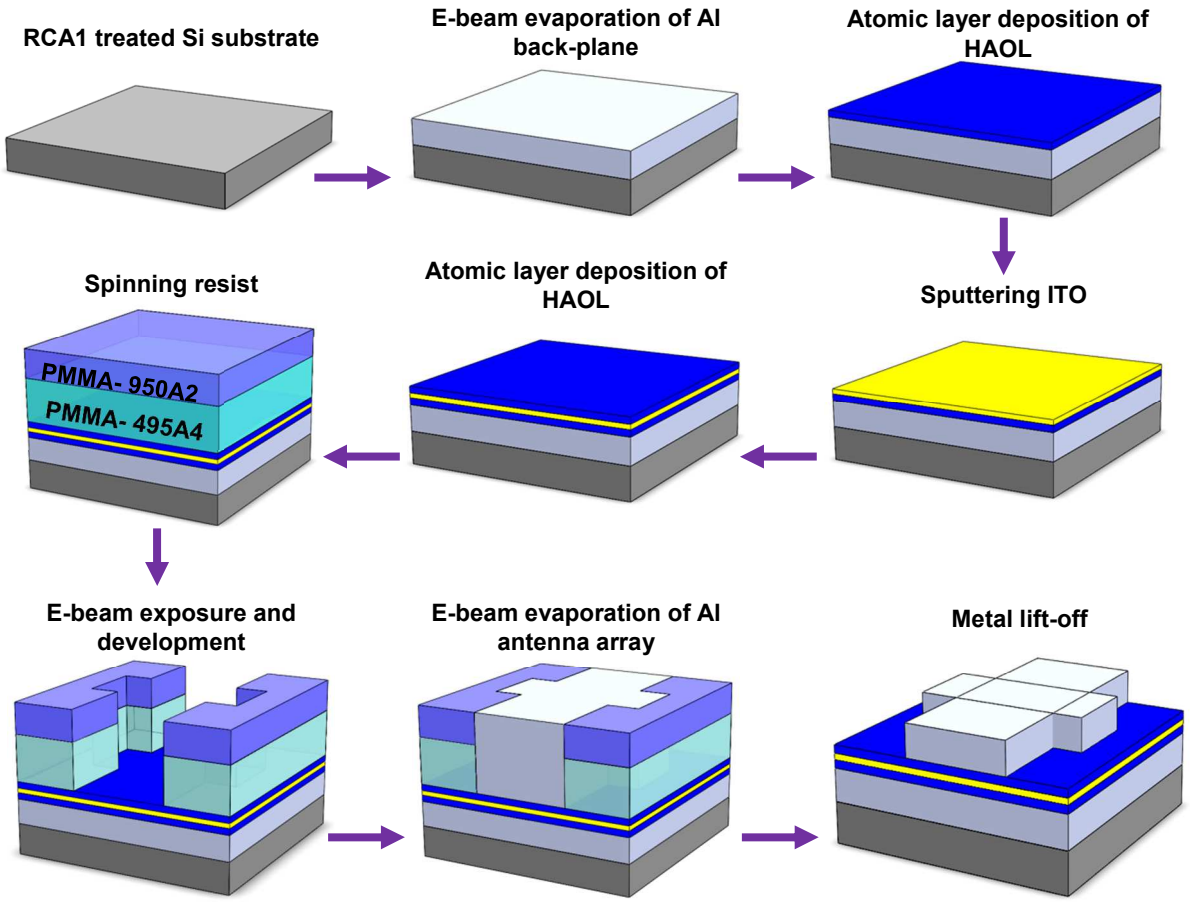

Figure S6. Schematic representation of fabrication steps of our dual-gated tunable metasurface.

6. Reflectance measurements

Figure S7 shows the experimental setup that we use for reflectance measurements. In our reflectance measurement setup, the metasurface is illuminated by a broadband laser. The laser beam impinges on the metasurface after passing through an optical chopper, a polarizer, a 50/50 non-polarizing beam splitter, and a 20x objective lens. We use a white light source, a flipping mirror and a CCD camera to make sure that the laser beam is positioned at the center of the metasurface. The light reflected from the metasurface is then guided to a Ge detector by the 50/50 beam splitter. The reflectance is obtained via

$$Reflectance\ [\%] = 100 \times \frac{R_{metasurface} - R_{background}}{R_{reference} - R_{background}} \quad \text{(S1)}$$

where $R_{metasurface}$ and $R_{reference}$ are the raw reflectance values obtained while illuminating the metasurface and the Al back reflector, respectively. $R_{background}$ is the background reflectance in the absence of incident laser beam.

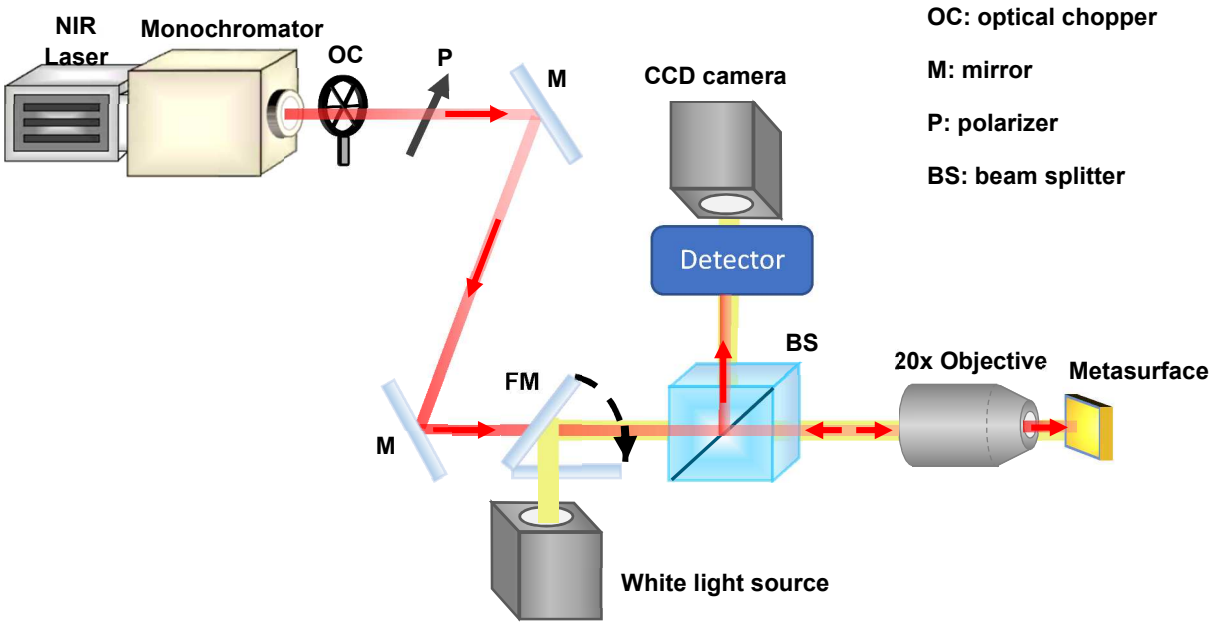

Figure S7. Optical setup for measuring the reflectance spectrum of our metasurfaces.

7. Phase shift measurements

We measure the phase shift of the light reflected from the tunable metasurface by using the optical setup shown in Figure S8. In this setup, the beam from a NIR tunable laser is directed towards the sample via a polarizer, a 50/50 non-polarizing beam splitter and then a 20x objective lens. The beam is positioned at the edge of the metasurface by using a white light source and a camera. As a result, the incoming beam is partly reflected from the metasurface and partly from the HAOL/ITO/HAOL/Al planar heterostructure. The light reflected from the sample is guided to the camera by using a 50/50 beam splitter. On the other hand, the laser beam itself is directed to the camera by using mirrors, where it serves as a reference beam. The camera records two regions of interference fringes i) the fringes formed via interference of the light reflected from the metasurface and the reference beam, and ii) the fringes formed via interference of the light reflected from the HAOL/ITO/HAOL/Al planar heterostructure and the reference beam.

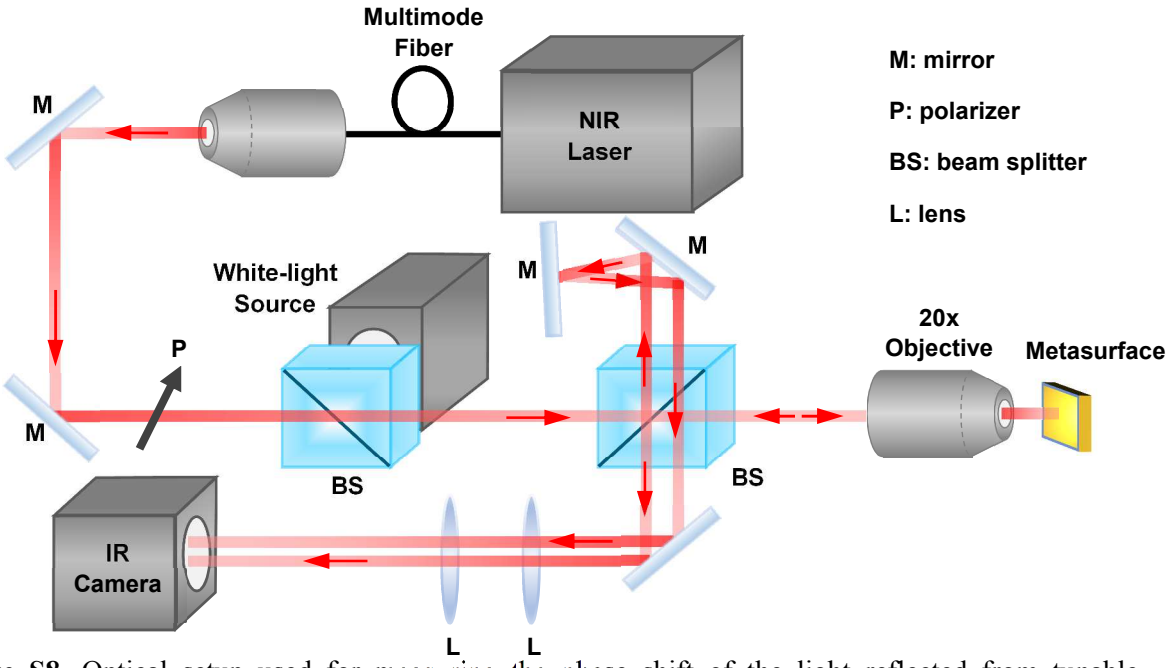

Figure S8. Optical setup used for measuring the phase shift of the light reflected from tunable metasurfaces.

To analyze the phase shift of the light reflected from our tunable metasurface, we process the images captured by the camera under different applied biases. In these images, we select one spatial cross section from the metasurface interference fringes and another one – from the reference fringes area. The intensity values at the cross sections are then interpreted as the curves which are then smoothened by a moving average (MA) filter. Figure S9a shows the interference fringes recorded by the NIR camera for different applied bias voltages. Figure S9b depicts the intensity data extracted from the reference fringes (indicated by **R**) and metasurface fringes (indicated by **M**). Figure S9b also plots MA-filtered curves for both reference and metasurface fringes. Figure S9c shows the sinusoidal functions fitted to the two mentioned fringe regions. Considering the offset between these two sinusoidal functions, one can calculate the phase shift for each applied bias via $Phase\ shift = \frac{\Delta p}{p_0}$, where Δp is the distance between the two fixed peaks of sinusoidal functions that correspond to the metasurface fringes and reference fringes, and p_0 is the period of the sinusoidal wave.

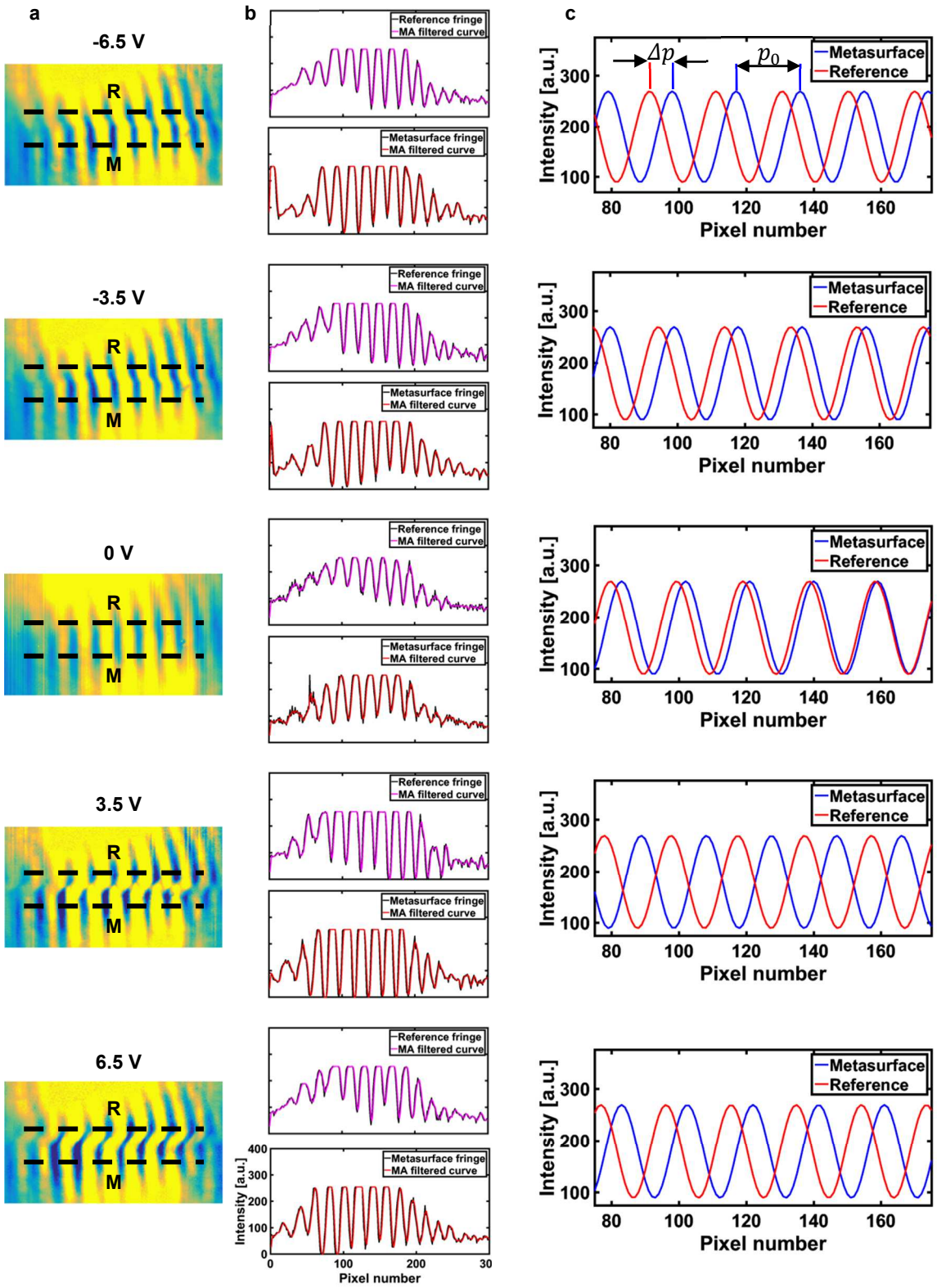

Figure S9. (a) The interference fringes captured by NIR camera. The dashed lines labeled **R** and **M** show the reference and metasurface fringe cross sections, respectively. (b) Extracted intensity data from reference and metasurface fringe cross sections and their MA smoothened curves. (c) Fitted sinusoidal waves for reference and metasurface fringe cross sections. Here, Δp is the distance between the two

fixed peaks of the sinusoidal functions fitted from metasurface and reference fringe cross sections, and p_0 is the period of the sinusoidal wave, respectively.

8. Comparison to single-gated tunable metasurface

To confirm that it is advantageous to use dual-gated metasurfaces as compared to single-gated ones, we calculate the phase shift of light reflected from the metasurface, when only the ITO layer and the fishbone antennas are biased with respect to each other. Figure S10a shows the reflectance as a function of wavelength and applied bias. Figure S10b, c plot reflectance and relative reflectance change spectrum for different applied voltages. The reflectance as a function of applied bias voltage for three different wavelengths close to the resonance wavelength is depicted in Figure S10d. Figure S10e shows the spectrum of the acquired phase. Figure S10f plots the phase shift as a function of applied voltage for wavelengths of λ =1545 nm, λ =1550 nm, and λ =1555 nm. As seen in Figure S10f, when we change the voltage from −6.5 V to +6.5 V, the phase shift changes from 58^o to -212.8^o for λ =1545 nm, from 75.6^o to −185.2^o for λ =1550 nm, and from 93^o to −156.8^o forλ =1555 nm. Therefore, the maximum achievable phase shift for the single-gated metasurface is ~271^o, which is 74^o smaller as compared to the phase shift obtained from the dual-gated metasurface. We note that the dual-gated metasurface exhibits an asymmetric response, enabling a given phase shift to be achieved via multiple different bias configurations, according greater flexibility in system design for beam steering.

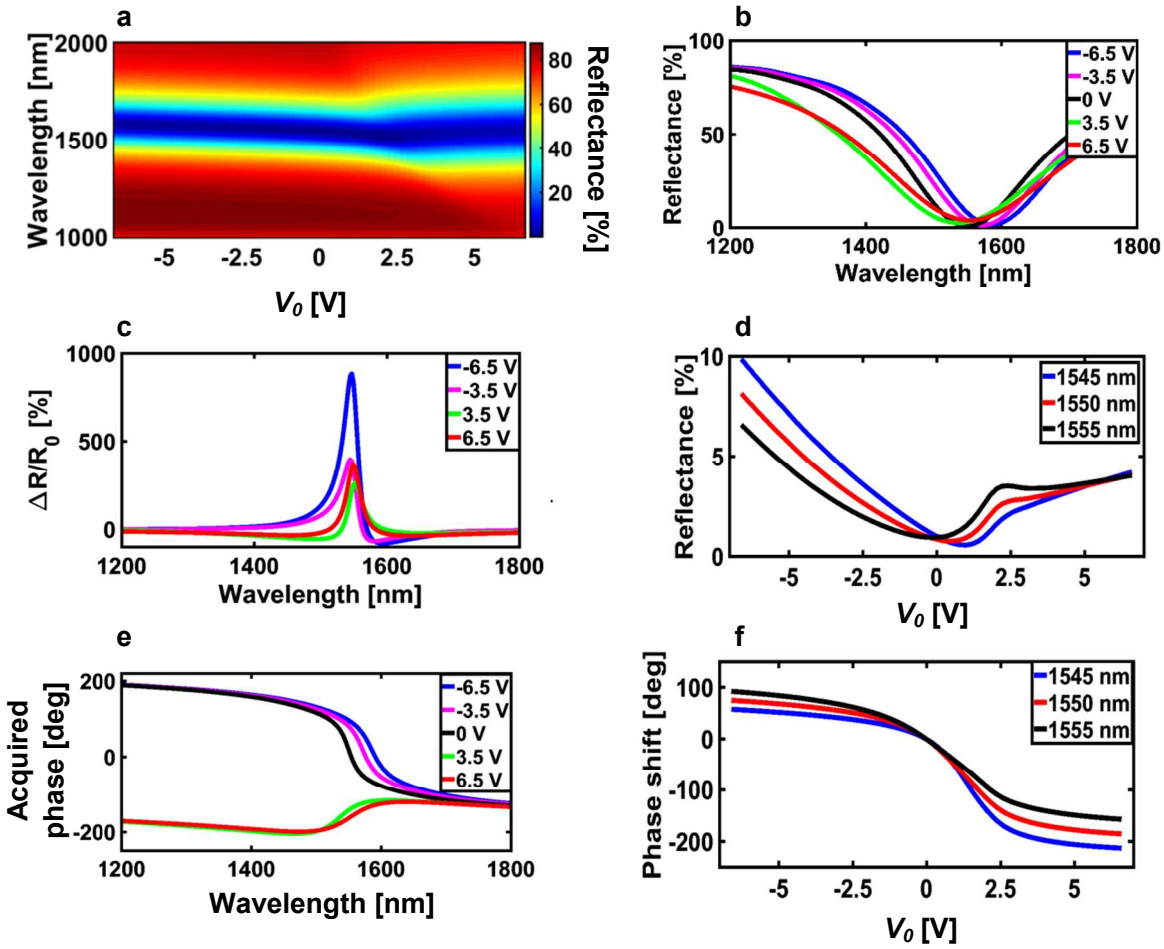

Figure S10: (a) Reflectance from the single-gated metasurface as a function of wavelength and applied bias, (b) reflectance and (c) relative reflectance change spectra for different applied voltages. (d) Reflectance from the single-gated metasurface as a function of applied bias voltage for three different wavelengths close to the resonance wavelength. (e) Spectra of the acquired phase for different applied biases. (f) Phase shift as a function of applied voltage at wavelengths mentioned in the legend of (d).

9. Effect of the ITO layer's thickness on the device tunability

In designing our dual-gated metasurface, the choice of the thickness of the ITO layer plays a crucial role in the amount of tunability our metasurface can provide. Figure S11 shows the maximum achievable relative reflectance change and maximum phase modulation obtained when changing the thickness of the ITO layer. As can be seen, increasing the thickness of the ITO layer will result in a smaller amount of achievable modulation. This means that the thinner the ITO layer, the more modulation can be achieved. On the other hand, we were not able to perform Hall measurement and ellipsometry fitting on ultra-thin ITO layers. As a result, we chose the thickness of ITO layer to be 5 nm.

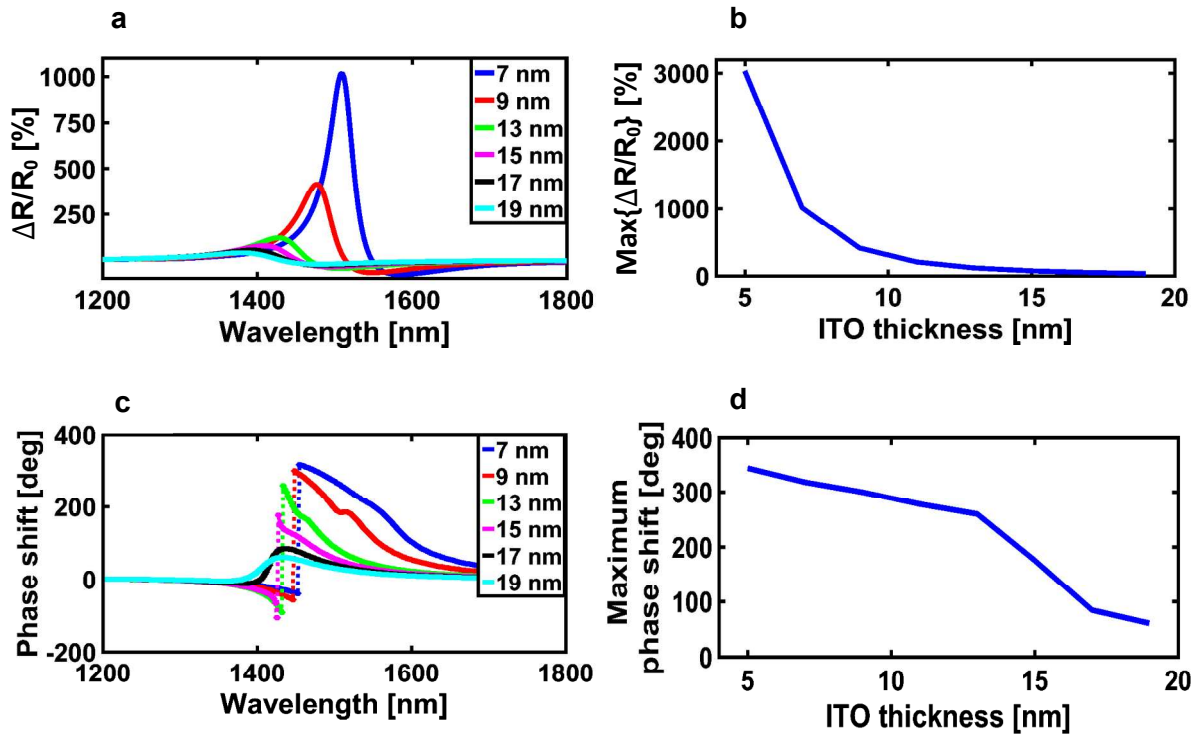

Figure S11: (a) Relative reflectance change spectrum for different thicknesses of the ITO layer, and (b) maximum achievable relative reflectance change as a function of ITO layer thickness (c) Phase shift spectrum for different thicknesses of the ITO layer, and (d) maximum achievable phase modulation as a function of ITO thickness.

The presented results provide evidence to the fact that further increase of the number of layers will not further increase the phase shift coverage. This is due to the fact that both the HfO_2/Al_2O_3 nanolaminate and the ITO layer have to be thicker than a specific lower limit in order to provide the desirable properties.

10. Theoretical demonstration of beam steering using the dual-gated metasurfaces

In the present section we use experimentally derived phase shift and reflectance values to theoretically estimate beam steering performance of our dual-gated metasurface. To steer the beam, we use a blazed grating approach. This implies that for each steering angle, we create a periodic phase pattern along the metasurface. In this approach, the period of the phase pattern is appropriately chosen to match the desired steering angle. We use the framework of antenna array theory to analytically calculate the far-field radiation pattern of our metasurface. In our analytical approach, we incorporate experimentally measured reflectance and phase shift values into the calculations of the far-field radiation pattern. Within the scope of the Fraunhofer approximation[10,11], the far-field intensity $I(\theta)$ can be analytically given as

$$I(\theta) = |E_{patt}|^2 \times |AF|^2, \quad \text{(S1)}$$

where E_{patt} is the far-field radiation pattern of a single metasurface element, while *AF* stands for the array factor. θ is the observation angle defined with respect to *z*-axis. Note that the reflected beam is steered in the *z*-*x* plane (see Fig. 1a). In our case, the array factor can be written as

$$AF = \sum_{j=1}^{N} \sqrt{R_j} e^{i((j-1)\, k\, d \sin(\theta) + \Phi_j)}. \quad \text{(S2)}$$

Here, j numerates the emitter, and N denotes the total number of emitters in the metasurface. k denotes the free space wave vector $k=2\pi/\lambda$, d gives the distance between neighboring emitters. Therefore, $(j-1)k\, d \sin(\theta)$ gives the phase difference conditioned by the path length difference to the observation point due to different emitter positions. Φ_j is the actively controlled emitter-imparted phase that controls the beam deflection. R_j gives the reflectance of the j^{th} emitter, which we extract from our measurement results (Figure 4). In this approach an emitter is defined as a scatterer, which scatters light with a given phase. For example, an emitter can be comprised of a single or multiple metasurface elements, depending on the voltage application configuration. The array factor captures the most important features of the far-field radiation pattern, such as the steering angle and the width of the steered beam. Since our emitter is relatively omnidirectional, we set $|E_{patt}| = 1$, and in what follows analyze the antenna factor only. In our calculations we assume that our metasurface consists of 100 elements, implying that in the case of our dual-gated metasurface, we can apply 200 independent bias voltages.

As mentioned above, we use a blaze grating approach to steer the beam. In this approach, we create a constant phase gradient along the metasurface, effectively creating a periodic phase pattern. Table S2 summarizes the experimentally derived voltages, which yield the relative phase shifts equal to 0^o, 90^o, 180^o, 270^o. The corresponding measured reflectance values are shown in the last column of Table S2. We define a grating blaze that consists of four metasurface elements with phase shifts of 0^o, 90^o, 180^o, 270^o. Since we assume that we have 100 metasurface elements, we can effectively create 25 blazes. In this case the parameter d equals to the period of our metasurface d=400 nm, which, and N=100. The calculated far-field radiation pattern shows that in this case the beam is steered to 72^o (Figure S12a). Next, we again employ four independent phase levels but now we define a single blaze as 0^o, 0^o, 90^o, 90^o, 180^o, 180^o, 270^o, 270^o. Note, that now in Eq. (2), we set d=800 nm, and N=48, implying that in this calculation we assume that the metasurface consists of 96 elements. In this case, our blazed grating consists of 12 blazes, and the steering angle is 28^o (Figure S12b).

We can also use six independent phase levels to demonstrate the beam steering. Table S3 summarizes the experimentally derived voltages, which yield the phase shifts equal to 0^o, 60^o, 120^o, 180^o, 240^o, and 300^o, which we use to define a unit blaze. In this case, d=400 nm, and N=96. The experimentally measured reflectance values are shown in the last column of Table S3. We can now apply 16 metasurface blazes that yields the steering angle of 39^o. As a final example, we define a unit blaze as 0^o, 0^o 60^o, 60^o, 120^o, 120^o, 180^o, 180^o, 240^o, 240^o, 300^o, 300^o. Thus, a single blaze consists of 12 metasurface elements. Note that in this case we set d=800 nm, and N=48. When this blaze is periodically applied, the reflected beam is steered to 19^o. The far-field radiation pattern of eight such blazes is shown in Figure S12d.

Table S2. Experimentally measured phase and reflectance values. The reported values of V_0 provide phase shift in 90^o steps.

Phase [^{o}]	Relative Phase [^{o}]	Voltage V_0 [V]	Reflectance [%]
-198.6	0	3.5	18.14
-108.6	90	1.3	13.51
-18.6	180	0.28	8.39
71.4	270	-3.1	21.58

Table S3. Experimentally measured phase and reflectance values. The reported values of V_0 provide phase shift in 60^o steps.

Phase [^{o}]	Relative Phase [^{o}]	Voltage V_0 [V]	Reflectance [%]
-211	0	5.5	19.64
-151	60	2.5	16.67
-91	120	1.35	13.42
-31	180	0.46	13.78
29	240	-1	17.75
89	300	-5.35	26.85

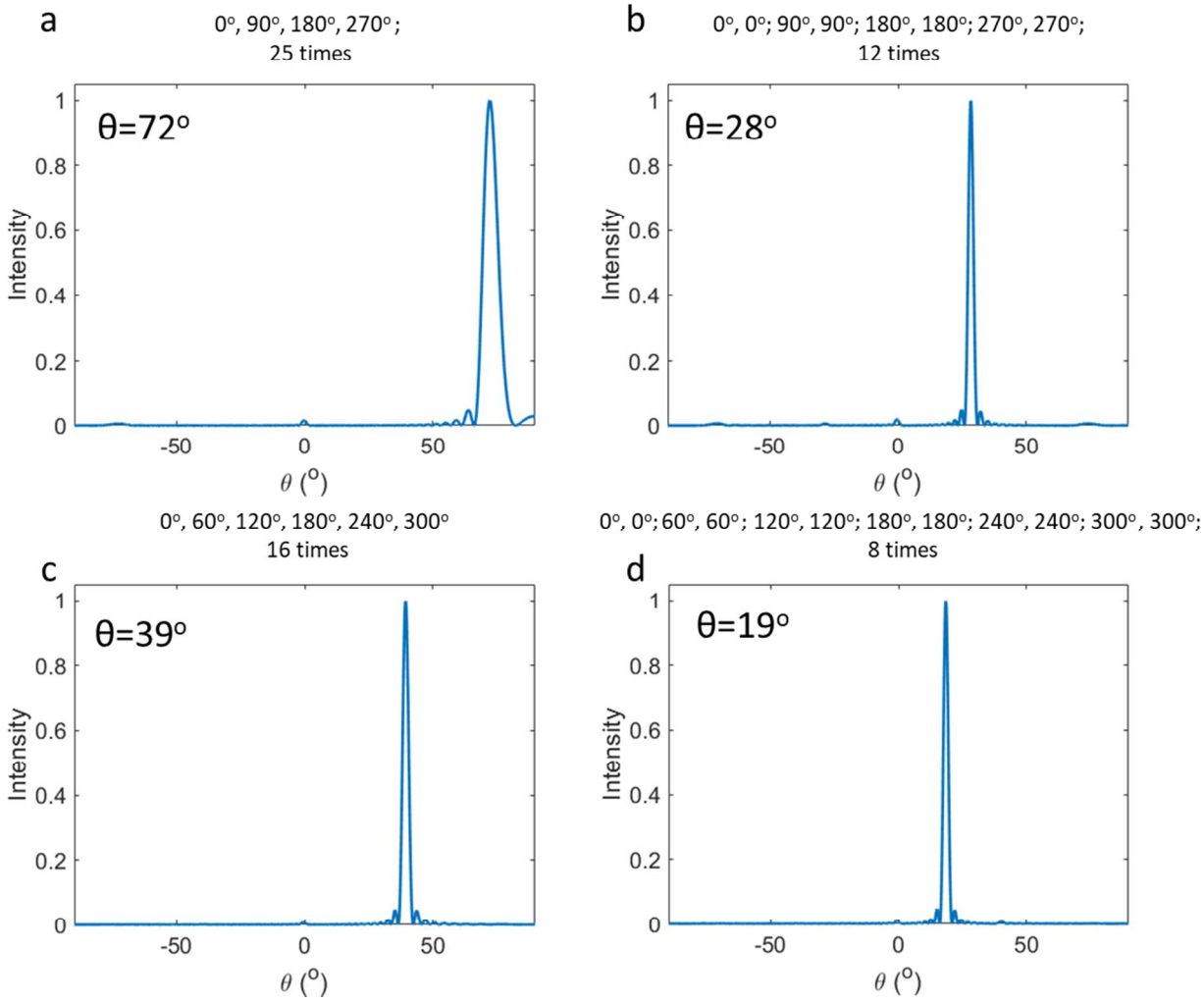

Figure S12: Far field radiation pattern for different voltage application configurations. The title of each subfigure specifies the phase profile of the metasurface. The inset of each subfigure cites the angle at which the beam is steered.

The steering angle θ obtained from Eqs. S1-S2 can also be calculated by using a simple grating equation:

$$\sin(\theta)=\lambda/L. \tag{S3}$$

Here, L denotes the length of the blaze. Using Eq. S3, we plot the steering angle as a function of the period of the blazed grating (Figure S3). Red dots in Figure S13 correspond to the blaze periods, which have been used to produce far-field radiation patterns shown in Figure S12. Dots **a**, **b**, **c**, **d**, correspond to Figures S12a, S12b, S12c, and S12d, respectively. The steering angles predicted by the grating equation S3 match well with the steering angles obtained from the calculations of the far-field radiation pattern. Thus, by using the blazed grating approach, we can also steer the beam to the other angles shown in Figure S13.

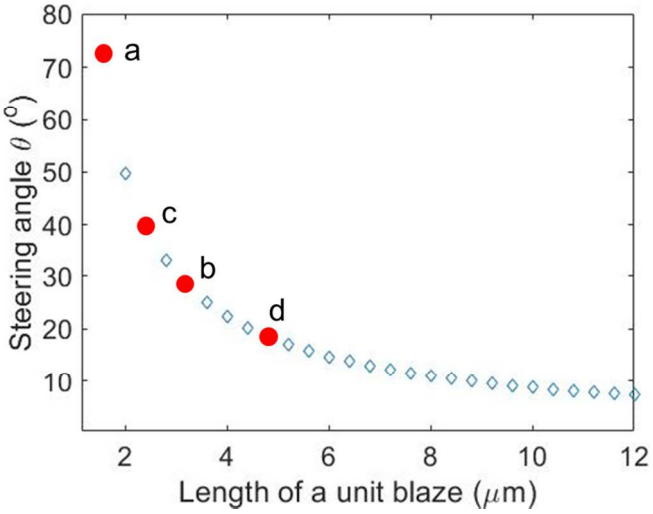

Figure S13: Steering angle as a function of the period of the blazed grating. Red dots correspond to the blaze periods, which were used to produce far-field radiation patterns shown in Figure S12. Dots **a**, **b**, **c**, **d**, correspond to Figures S12a, S12b, S12c, and S12d, respectively.

References

1. Klein, A.; Korber, C.; Wachau, A.; Sauberlich, F.; Gassenbauer, Y.; Harvey, S. P.; Proffit, D. E.; Mason, T. O. *Materials* **2010,** 3, 4892-4914.
2. Yi, F.; Shim, E.; Zhu, A. Y.; Zhu, H.; Reed, J. C.; Cubukcu, E. *Appl Phys Lett* **2013,** 102.
3. Cao, D.; Cheng, X.; Zheng, L.; Xu, D.; Wang, Z.; Xia, C.; Shen, L.; Yu, Y.; Shen, D. *J. Vac. Sci. Technol. B* **2015,** 33.
4. Feigenbaum, E.; Diest, K.; Atwater, H. A. *Nano Lett.* **2010,** 10, 2111-2116.
5. Lee, H. W.; Papadakis, G.; Burgos, S. P.; Chander, K.; Kriesch, A.; Pala, R. A.; Peschel, U.; Atwater, H. A. *Nano Lett.* **2014,** 14, 6463-6468.
6. Kim, J. S.; Cacialli, F.; Cola, A.; Gigli, G.; Gingolani, R. *Synthetic Met 2000* 111, 363-367.
7. Melikyan, A.; Lindenmann, N.; Walheim, S.; Leufke, P. M.; Ulrich, S.; Ye, J.; Vincze, P.; Hahn, H.; Schimmel, T.; Koos, C.; al., e. *Opt. Express* **2011,** 19, 8855-8869.
8. Michelotti, F.; Dominici, L.; Descrovi, E.; Danz, N.; Menchini, F. *Opt. Lett.* **2009,** 34, 839-841.
9. Bayer, T. J. M.; Wachau, A.; Fuchs, A.; Deuermeier, J.; Klein, A. *Chemistry of Materials* **2012,** 24, 4503-4510.
10. J. Goodman, *Introduction to Fourier Optics* (McGraw-Hill, 1996).
11. Sherrott, M. C.; Hon, P. W. C.; Fountaine, K. T.; Garcia, J. C.; Ponti, S. M.; Brar, V. W.; Sweatlock, L. A.; Atwater, H. A. *Nano Lett.* **2017,** 17, 3027-3034.